A. Yeganeh-Bakhtiary[1]
Enviro-Hydroinformatics COE
and School of Civil Engineering,
Iran University of Science & Technology (IUST),
Tehran 16846-13114, Iran;
Hydro-environmental Research Centre,
School of Engineering,
Cardiff University,
Queen's Buildings,
The Parade Cardiff,
Wales CF24-3AA, UK
e-mail: yeganeh@iust.ac.ir & yeganeh@cf.ac.uk

M. Zanganeh

E. Kazemi

School of Civil Engineering,
IUST,
Tehran 16848-13114, Iran

L. Cheng
School of Civil and Resource Engineering,
The University of Western Australia,
Perth, WA 6009, Australia

A. K. Abd Wahab
Coastal & Offshore Engineering Institute,
Universiti Teknologi Malaysia (UTM),
International Campus,
Kuala Lumpur 54100, Malaysia

Euler–Lagrange Two-Phase Model for Simulating Live-Bed Scour Beneath Marine Pipelines

In this study, an Euler–Lagrange coupling two-phase flow model, namely movable bed simulator (MBS)-two-dimensional (2D) model was employed to explore the current-induced live-bed scour beneath marine pipelines. The fluid phase characteristics, such as velocity and pressure, were obtained by the Reynolds-averaged Navier–Stokes (RANS) equations with a k-ε turbulence closure model in a two-dimensional Eulerian grid, whereas the seabed beneath pipelines was traced as an assembly of discrete sand grains from the Lagrangian point of view. The live-bed scour was evolved as the motion of a granular media based on distinct element method (DEM) formulation, in which the frequent interparticle collision was described with a spring and dashpot system. The fluid flow was coupled to the sediment phase, considering the acting drag forces between. Comparison between the numerical result and experimental measurement confirms that the numerical model successfully estimates the bed profile and flow velocity field. It is evident that the fluid shear stress decreases with the increasing of gap ratio e/D. The numerical model provides a useful approach to improve mechanistic understanding of hydrodynamic and sediment transport in live-bed scour beneath a marine pipeline. [DOI: 10.1115/1.4023200]

Keywords: current flow, distinct element method (DEM), Euler–Lagrange coupling, live-bed scour, marine pipelines, movable bed simulator (MBS) model, two-phase model

1 Introduction

Laying pipelines on seabed versus unidirectional current induces the disturbance of flow pattern and results in the local scouring beneath marine pipelines. Estimation of local scouring is a crucial issue in design and maintenance of marine pipelines in the sandy bed condition. The process of current-induced scour can be categorized in three stages happening subsequently: onset of scour, tunnel erosion, and lee-wake erosion [1]. The onset of scour depends on the seepage flow in the seabed and finally results in a hole beneath a marine pipeline. After emergence of the initial scour hole, the sudden increase in flow shear stress, causing a rapid bed sediment motion, and the local scouring undergoes to the tunnel erosion stage. The final stage of scour is the lee-wake erosion, which is attributed to vortex-shedding after the mound formation at the rear side of the pipe and quantitatively related to the Strouhal number (see Fig. 1).

There are a vast variety of experimental studies on the current-induced flow pattern around a pipe in both loose and rigid beds (e.g., Refs. [1–8]). Mao's [5] experiment has been employed so far as the benchmark test for calibration and comparison of the numerical simulation efforts. The experimental investigations usually bring a heavy cost for physical modeling of the phenomenon, and its application is not straightforward to extend to different hydrodynamics conditions.

On the other hand, the numerical simulation can be employed as an alternative tool to study the scour process beneath a pipe, because of its flexibility toward several conditions. Recently, several single-phase numerical methods have been developed to estimate the equilibrium scour depth and/or evolution of scour. These models can be categorized either as the potential flow theory or viscous/turbulent flow theory. The potential flow-based models not only were not generally able to model the flow separation and vortex shedding, but also they were not able to estimate the correct scour profile [9,10]. To deal with the shortcoming of the potential flow model, some efforts are devoted to simulate the viscous-based models, in which the turbulence models, e.g., the k-ε and/or k-ω turbulence models are closured with the Reynolds-averaged Navier–Stokes (RANS) solver, while the bed profile evolution is performed by the sediment mass conservative equation [11,12]. Dupuis and Chopard [13] applied the Lattice Boltzmann method for simulation of current-induced scour. The results proved that the model performed reasonably for estimating the scour profile evolution versus the experimental observations.

Since the single-phase model usually was not able to consider interparticle interactions in the scour beneath a pipe, to cope with this problem more recently, some researchers developed the so-called Euler–Euler coupling two-phase flow approach to simulate the scour process as the two-phase flow media [14,15]. In the Euler–Euler coupling two-phase flow models, the fluid and sediment phases are treated as separate continuous mediums. The coupling between the fluid and sediment phases is described with properly considering the fluid-particle and interparticle interactions between phases. The continuum model is potentially a powerful tool, because it considers each physical element in the form of conservation equations. The Euler–Euler coupling model, nevertheless, sidesteps probabilistic characteristics involving the motion of sediment particles. Significant deficiencies may be, therefore, associated with the Euler–Euler coupling models, provided that such a probabilistic nature becomes important. As Yeganeh et al. [16] pointed out, the probabilistic character of

[1]Corresponding author.

Contributed by the Ocean, Offshore, and Arctic Engineering Division of ASME for publication in the JOURNAL OF OFFSHORE MECHANICS AND ARCTIC ENGINEERING. Manuscript received September 20, 2010; final manuscript received March 4, 2012; published online June 10, 2013. Assoc. Editor: Colin Leung.

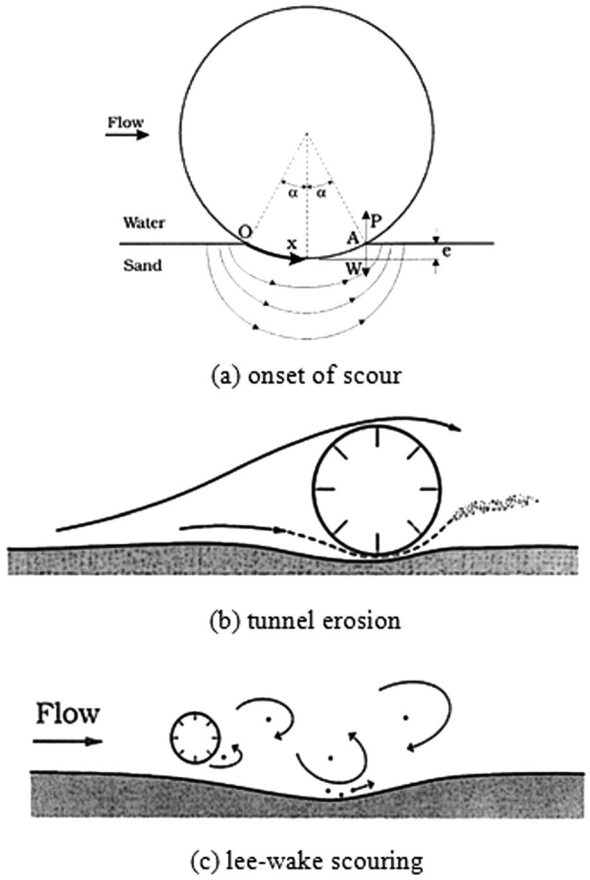

Fig. 1 Different stages of scouring beneath pipeline [23]

moving bed sediment can be described well with the aid of a Lagrangian model. In the Lagrangian model, the following key points should be included: the random motion of sediment particles with irregular interparticle collision; the interphase momentum exchange; and the momentum transfer during the interparticle collision. Regarding the numerical simulation, the Euler–Lagrange coupling two-phase flow models requires greater computational run time and vastly increased memory relative to the Euler–Euler coupling models.

The Euler–Lagrange coupling approach as a new method has been applied by many researchers to sediment transport simulation. In these models, the governing equations of fluid phase are described as a continuum media in the Eulerian form, while the governing equations of sediment phase are based on the Lagrange form accompanied with tracking the sediment particle. Calantoni et al. [17] applied an Euler–Lagrange coupling approach for simulation of sediment transport in the nearshore region. Their model contains the discrete particle method (DPM) for simulating sediment phase and the finite volume method (FVM), adopted for discretizing the fluid phase. The flow and sediment interaction was considered in the one-way state in terms of its simplicity and applicability in the studied case. Yeganeh-Bakhtiary et al. [18] also employed an Euler—Lagrange coupling model to simulate sediment transport at the high bottom shear in a unidirectional flow condition.

The main objective of this study is to investigate the capability of the Euler–Lagrange coupling model for simulation of current-induced live-bed scour beneath marine pipelines as a two-phase media. It is focused on the flow hydrodynamics that influences the tunnel erosion and lee-wake stages of the scour processes beneath a pipe, considering the flow-particle interaction and interparticle interaction in a two-way coupling manner and studying the corresponding scour profile in the framework of the MBS-2D two-phase model. At first, the fluid phase model was validated against the experimental study of Alper Oner et al. [8] for current flow around a pipe over a fixed bed. Then, numerical results were compared with the experimental data of Mao [5], which is usually used as a benchmark test for simulation of scour beneath pipelines.

This paper is presented in the four following sections: after the introduction, Sec. 2 outlines the mathematical formulation of the fluid-phase model, including the governing equations and its boundary conditions. In Sec. 3, the fluid phase model efficiency against the conducted experiments by Alper Oner et al. [8] is examined. Then, the hydrodynamic of the flow influencing the different stages of the scour beneath a pipe are numerically investigated. In Sec. 4, the mathematical formulation of the sediment phase is explained, following the description of the interparticle interaction model and the computational domain and boundary condition. Finally, the MBS-2D results are compared with the experimental data, and the characteristics of current-induced live-bed scour are discussed.

2 Formulation of Fluid Phase Model

In the following, the essential details of the fluid phase model are described.

2.1 Governing Equation of Fluid Phase. The fluid phase is developed based on the Reynolds-averaged Navier–Stokes (RANS) equations, closured with a k-ε turbulence model. The governing equations consist of the continuity and momentum together with the equations for turbulent kinetic energy k and turbulence dissipation rate ε in the two-dimensional coordinates as follows:

$$\frac{\partial U}{\partial x}+\frac{\partial V}{\partial y}=0 \tag{1}$$

$$\frac{\partial U}{\partial t}+U\frac{\partial U}{\partial x}+V\frac{\partial U}{\partial y}=-\frac{1}{\rho}\frac{\partial P}{\partial x}+\frac{\partial}{\partial x}\left[2\Gamma\frac{\partial U}{\partial x}\right]+\frac{\partial}{\partial y}\left[\Gamma\left(\frac{\partial U}{\partial y}+\frac{\partial V}{\partial x}\right)\right]-\frac{F_{Dx}}{\rho} \tag{2}$$

$$\frac{\partial V}{\partial t}+U\frac{\partial V}{\partial x}+V\frac{\partial V}{\partial y}=-\frac{1}{\rho}\frac{\partial P}{\partial y}+\frac{\partial}{\partial x}\left[\Gamma\left(\frac{\partial U}{\partial y}+\frac{\partial V}{\partial x}\right)\right]+\frac{\partial}{\partial y}\left(2\Gamma\frac{\partial V}{\partial y}\right)-\frac{F_{Dy}}{\rho}+g \tag{3}$$

$$\frac{\partial k}{\partial t}+U\frac{\partial k}{\partial x}+V\frac{\partial k}{\partial y}=\frac{\partial}{\partial x}\left[\left(\nu+\frac{\nu_t}{\sigma_k}\right)\frac{\partial k}{\partial x}\right]+\frac{\partial}{\partial y}\left[\left(\nu+\frac{\nu_t}{\sigma_k}\right)\frac{\partial k}{\partial y}\right]+p_r-\varepsilon \tag{4}$$

$$\frac{\partial \varepsilon}{\partial t}+U\frac{\partial \varepsilon}{\partial x}+V\frac{\partial \varepsilon}{\partial y}=\frac{\partial}{\partial x}\left[\left(\nu+\frac{\nu_t}{\sigma_\varepsilon}\right)\frac{\partial \varepsilon}{\partial x}\right]+\frac{\partial}{\partial y}\times\left[\left(\nu+\frac{\nu_t}{\sigma_\varepsilon}\right)\frac{\partial \varepsilon}{\partial y}\right]+\frac{\varepsilon}{k}(c_{1\varepsilon}p_r-c_{2\varepsilon}\varepsilon) \tag{5}$$

$$p_r=\nu_t\left[2\left(\frac{\partial U}{\partial x}\right)^2+2\left(\frac{\partial V}{\partial y}\right)^2+\left(\frac{\partial U}{\partial x}+\frac{\partial V}{\partial y}\right)^2\right] \tag{6}$$

$$\Gamma=\nu+\nu_t;\quad \nu_t=C_\mu\frac{k^2}{\varepsilon} \tag{7}$$

where U and V are mean flow velocity components in horizontal and vertical directions, respectively; P is the pressure; t is the time marching in the fluid phase; Γ is the effective viscosity; ν is the molecular kinetic viscosity; ν_t is the eddy viscosity; k is the turbulent kinetic energy; ε is the dissipation of turbulent kinetic energy; p_r is the production of turbulent kinetic energy due to shear stress; g is the acceleration of gravity; and C_μ, σ_k, σ_ε, $C_{1\varepsilon}$, and $C_{2\varepsilon}$ are constants in the $k-\varepsilon$ turbulence model. The turbulence model constants are set according to Launder and Spalding [19] and reported in Table 1. $F_{Dx}=\sum_i f_{Dx_i}$ and $F_{Dy}=\sum_i f_{Dy_i}$ are the sediment-fluid interactions terms in the horizontal and vertical directions, respectively where f_{Dx_i} and f_{Dy_i} are the sediment-fluid

Table 1 Constants for the *k*-ε turbulence closure model

C_μ	σ_k	σ_ε	$c_{1\varepsilon}$	$c_{2\varepsilon}$
0.09	1.0	1.3	1.44	1.92

Table 2 Constants for the sediment phase in the MBS-2D model

A_2	A_3	C_M	$C_{D\infty}$
$\pi/4$	$\pi/6$	0.5	0.4

interaction terms in the horizontal and vertical directions for particle i, respectively. These are calculated based on the sediment particles existing in the related cell. It is noted that implementation of the sediment-fluid interactions terms is justified by Snider et al. [20] in the modeling of multiphase dense flows, the same condition as the live-bed scour beneath the pipelines.

2.2 Boundary Conditions. Figure 2 shows the inlet and outlet boundaries located at $10D$ and $20D$, far from the pipe center, respectively. At the inlet boundary, a fully developed turbulent velocity profile is applied,

$$U(y) = \frac{u_*}{\kappa}\ln\left(E\frac{u_* y}{\nu}\right); \quad V(y) = 0.0 \tag{8}$$

where u_* is the shear velocity ($=\sqrt{\tau_w/\rho}$); τ_w is the shear stress in the flow direction,κ is the von Karman constant (=0.41), and E (≈9.0) is a constant value [21]. Zero normal gradients of all parameters except pressure are applied at the outlet boundary. At the bottom, the wall function is used to account for the rough bed, and the gradient of averaged velocity is expressed as follows (see, among others, Refs. [11,22]:

$$\frac{\partial U(z)}{\partial z} = \frac{u_*}{\kappa z} \tag{9}$$

Here, z is the distance of the first grid from the bed. If the above equation is integrated, the logarithmic velocity distribution at the boundary layer is obtained. Using the final value of shear velocity, u_*, the boundary values of k and ε at the bed can be defined as follows:

$$\varepsilon = \frac{u_*^3}{\kappa y\left[1-\exp\left(-\frac{u_* z}{26\nu_t}\right)\right]} \tag{10}$$

$$\nu_t = \kappa u_* y\left[1-\exp\left(-\frac{u_* z}{26\nu}\right)\right] \tag{11}$$

$$k = \frac{u_*^2}{\sqrt{C_\mu}} \tag{12}$$

The water surface is assumed far enough from the cylinder. Therefore, it can be assumed that the effects of blocking vortex shedding on the water surface are negligible [11]. Hence, the symmetric boundary condition was employed, in which the vertical velocity and the gradient of horizontal velocity at the vertical direction were zero (see Fig. 2).

The governing equations of fluid phase are discretized on a staggered mesh, in which the fluid pressure, turbulent kinetic energy, and dissipation rate are defined at the center of the scalar cell. The fluid velocities are defined at the center of the staggered cell, which is positioned at the scalar cell faces. The governing equations are solved in a Cartesian coordinate by the finite volume method with the SIMPLE algorithm. The hybrid scheme is applied to approximate the discretized equations: the convection and the diffusion terms are discretized with the first order upwind and second order central differencing schemes, respectively.

3 Modeling of Fluid Flow

It is attempted to validate the fluid model against the experimental studies of Alper Oner et al. [8] for velocity profiles around the pipe, both qualitatively and quantitatively. In their experimental setup, a transparent Plexiglas-walled laboratory channel was used with 1 m width, 0.75 m depth and 14 m length. The water depth in the channel and pipe diameter was, respectively, 0.6 m and 0.05 m, and the current velocity was 19.7 cm/s. The first, qualitative validation was closely related to the distribution of velocity at the front and rear side of the pipe, as shown particularly in the boundary layer context [8]. The computational domain was set to $30D$ long and $3.5D$ depth, as shown in Fig. 2. It is noted that the dimensions of computational domain were chosen based on the Liang and Cheng [11] recommendation to cover the complete vortex-shedding domain. The pipe was located at $10D$ on the seabed, and 1500×260 grids were considered to discrete the computational domain.

The comparison of the simulated and measured mean horizontal velocity around a pipe with $\mathrm{Re_D} = 9500$ for two cases of $e/D = 0$ and $e/D = 0.3$ at the various cross-sections is depicted in Fig. 5. The grid size near the bottom wall was refined to capture the high variation of flow characteristics near the pipe for both cases. As seen, the model describes the horizontal velocity profile at the upstream and downstream of the pipe very well. A great deal in modeling of scour beneath pipelines is the analysis of flow pattern around pipelines laid on the bed ($e/D = 0.0$); hence, the calculated fluid pattern in terms of time-averaged streamlines is shown in Fig. 4. To compare qualitatively the simulation result with the experiments, the experimental data of Alper Oner et al. [8] are also presented at the top of the figure. As can be seen, the pattern of simulated flow streamlines is identical to the experimental one. The simulated and experimental results for the time-averaged streamlines and its pair of primary vortices at the rear side of the pipe are clearly similar. However, size of vortices at the front and rear sides of the pipe is a little smaller than the observations, which may be attributed to the mesh density near the pipe surface. It can be concluded that the numerical model results share a very good agreement with the Alper Oner et al. [8] experiment.

An important characteristic of the current flow around a pipe is the vortex shedding that affects the live-bed scour. Thus, by simulating one of Alper Oner et al.'s [8] experimental conditions ($\mathrm{Re_D} = 9500$ and $e/D = 0.3$), the model capability in the modeling of vortex shedding is examined and shown in Fig. 5. According to Sumer and Fredsøe [1], the vortex shedding takes place when the pipe is far enough from the bed that the lower shear layer can be developed as strongly as the upper shear layer of the pipe, which

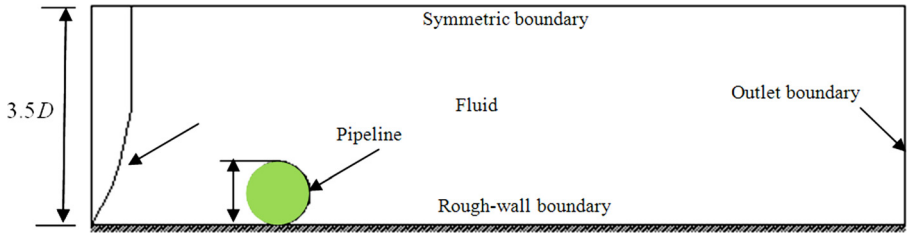

Fig. 2 Schematic sketch of the computational flow domain

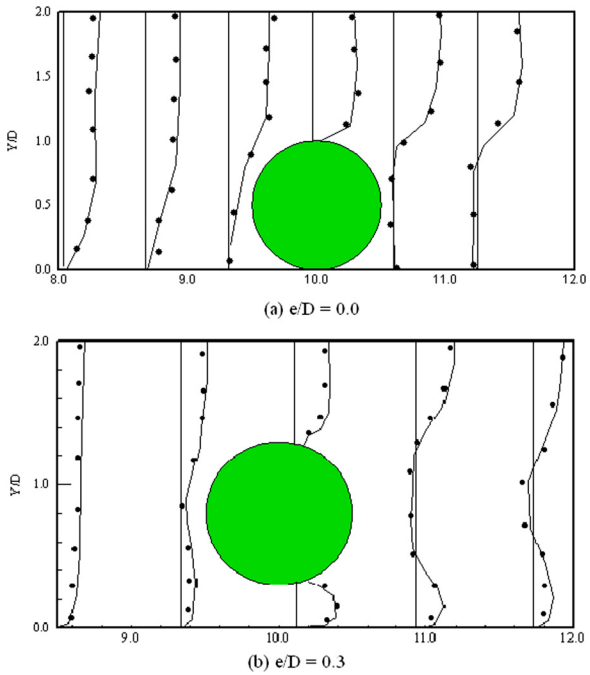

Fig. 3 Comparison of the mean horizontal velocity of numerical result with Alper Oner et al. [8] experimental data at $Re_D = 9500$: (*a*) $e/D = 0.0$ and (*b*) $e/D = 0.3$. The experimental data are presented by symbols and the model results denoted by solid line.

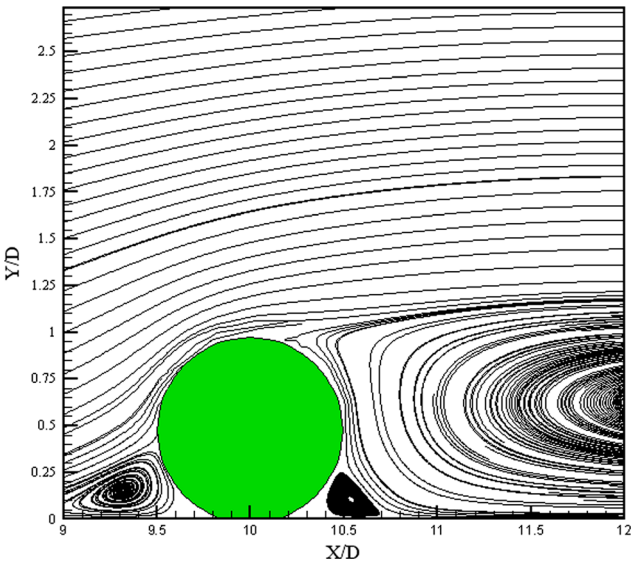

Fig. 4 Time-averaged streamlines for $Re_D = 9500$ and $e/D = 0$ at the top of the figure for the experimental result of Alper Oner et al. [8]

leads to a strong interaction between the shear layers and, subsequently, suppression of the vortex shedding. Figure 5 shows the snapshots of instantaneous streamlines around the pipe at different time instants. As seen, the vortex formation and the shedding process are readily presented in the figure. Two vortices at the upper and lower sides of the pipe were formed in a periodic manner with a certain time lag. The qualitative comparison of the simulated vortex shedding with the experiment indicates that the flow model is capable of simulating the vortex shedding. Comparison between the simulation and experimental results shown in Figs. 3–5 demonstrates the model capability of simulating the current flow near a pipe where vortex shedding occurs.

In this part, it is attempted to employ the fluid phase model to explore some sophisticated hydrodynamic parameters, such as flow velocity near the pipe, fluid shear stress, and Strouhal number, with measurements that are rather difficult and time-consuming. These parameters respectively influence the different stages of the scour processes beneath a pipeline.

Figure 6 displays the time fluctuation of flow horizontal velocity during the vortex shedding process at upper and down sides of the pipe, the same condition presented in Fig. 5. It is expected that the fluctuation in flow horizontal velocity during the vortex shedding happens with a time lag. As seen, the horizontal velocity at the upper side of the pipe after its initial maximum value reaches its minimum when the free-stream side vortex gradually is convected and shed towards downstream from the pipe surface at $t = 0.5$ s, corresponding to the condition shown in Fig. 5(*a*). Simultaneously, the down side horizontal velocity after its initial value reaches to its local maximum while the lower shear layer becomes gradually stronger. Whereas, at $t = 1.0$ s (see Fig. 5(*b*)), the down side horizontal velocity reaches its local minimum as the lower shear layer becomes stronger and the bottom side vortex starts to be generated. At $t = 2.0$ s to the end of the vortex shedding process (see Figs. 5(*c*)–5(*f*)), both the upper and down sides of the velocities become rather steady, and consequently, the lower shear layer little by little is developing to become as strong as the upper shear layer of the pipe. This leads to a strong interaction between the shear layers and subsequently suppression of the vortex shedding.

Figure 7 displays the distribution of fluid bottom shear stress along the seabed for different gap ratios. The bottom shear stress is calculated by

$$\tau_w = \mu \frac{dU}{dy} \tag{13}$$

in which τ_w is the fluid shear stress along the bottom wall. As can be seen from the figure, the fluid shear stress increased with decreasing e/D at the pipe vicinity, and it reaches to its maximum value at the gap beneath the pipe center. As expected, the fluid shear stress converges to a fix value of live-bed condition at a distance far from the pipe. At small gap ratios, flow in the gap between the rough bed and pipe is very strong, and the flow is similar to a jet flow [1]. Therefore, the jet velocity beneath the pipe at $e/D = 0.1$ is the largest in the gap. The mechanism of flow shear stress can be attributed to the vortex generated at the front and rear sides of the pipe. As Yeganeh-Bakhtiary [15] pointed out at small gap ratios, a small eddy, which rotates clockwise, generates in front of the pipe, which is also in line with the experimental findings (among others, see Refs. [4,24,25]). It partly deflects approaching flow away from the gap and, consequently, reduces the flow passing through the gap. In other words, the eddy at the front side of the pipe just forms an obstruction to the approaching flow near the bed and decreases the fluid shear stress at the front side of pipe. However, the gap flow is not significantly affected by the eddy at the rear side of pipe that is mainly moved upwards behind the pipe; thus, the fluid shear stress increases noticeably here. By increasing the gap ratios, the eddy at the front side of the pipe becomes weak and ultimately disappears. Moreover, two eddies are seen just behind the pipe and may interact noticeably and create the vortex shedding.

Figure 8 illustrates the power spectral density (PSD) diagram for horizontal velocity around a pipe with $Re_D = 9500$ and $e/D = 0.3$. It is intended to obtain the pipe's Strouhal number based on the frequency of vortex shedding that can be evaluated by using the technique of PDS analysis of the flow velocity (for more information, see Ref. [8]). The Strouhal number is estimated as

$$St = \frac{fD}{U_0} \tag{14}$$

Here, f is the vortex-shedding frequency, U_0 is the current velocity, and D, as previously mentioned, is the pipe diameter. It is evident from Fig. 8 that the value of PSD for both the upper and lower sides of the pipe is maximum in a frequency equal to 0.625 that is corresponding to a Strouhal number equal to 0.158

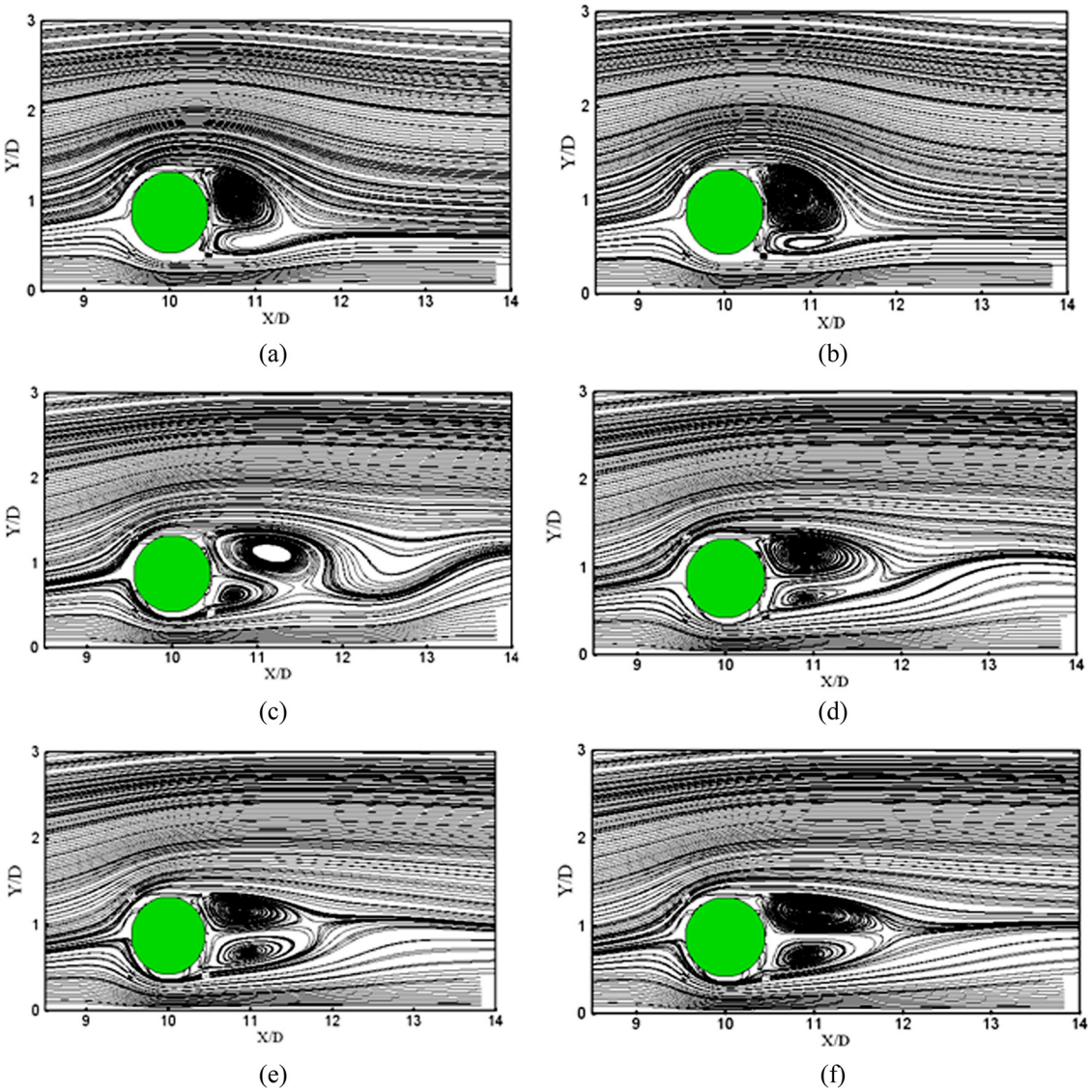

Fig. 5 Snapshots of instantaneous streamlines for $Re_D = 9500$ and $e/D = 0.3$ within $t = 4.5$ s; (*a*) $t = 0.5$ s, (*b*) $t = 1.0$ s, (*c*) $t = 2.0$ s, (*d*) $t = 3.0$ s, (*e*) $t = 4.0$ s, and (*f*) $t = 4.5$ s

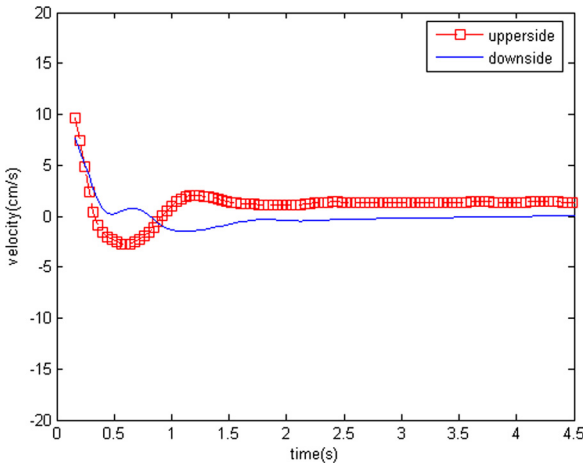

Fig. 6 Time variation of horizontal flow velocity at upper and downsides of pipe

according to Eq. (14). This value for the Strouhal number is very close to the value obtained by Alper Oner et al. [8] for their experiment case of $e/D = 0.3$.

4 Formulation of Sediment Phase Model

4.1 Governing Equation of Sediment Phase. The sediment phase in MBS-2D was constructed as a Lagrange approach based on the Cundall and Strack [26] initial idea for simulation of discrete elements in rock mechanics, introducing the soft contact among each contacting particles. The sediment particles were treated as rigid disks with the uniform diameters in a vertically two-dimensional plane, and the equations of motion of the i_{th} particle on the vertically 2D coordinates are as follows:

$$\rho\left(\frac{\rho_s}{\rho}+C_M\right)A_3 d^3\frac{du_{pi}}{dt}=\sum_j\left[-f_n\cos\alpha_{ij}+f_s\sin\alpha_{ij}\right]+f_{Dx_i}$$

$$\text{here}\quad f_{Dx_i}=\frac{\rho}{2}C_D A_2 d^2\sqrt{(U-u_{pi})^2+(V-v_{pi})^2}\,(U-u_{pi}) \tag{15}$$

$$\rho\left(\frac{\rho_s}{\rho}+C_M\right)A_3 d^3\frac{dv_{pi}}{dt}=\sum_j\left[-f_n\sin\alpha_{ij}+f_s\cos\alpha_{ij}\right]-\rho\left(\frac{\rho_s}{\rho}-1\right)gA_3 d^3+f_{Dy_i}$$

$$\text{here}\quad f_{Dy_i}=\frac{\rho}{2}C_D A_2 d^2\sqrt{(U-u_{pi})^2+(V-v_{pi})^2}\,(V-v_{pi}) \tag{16}$$

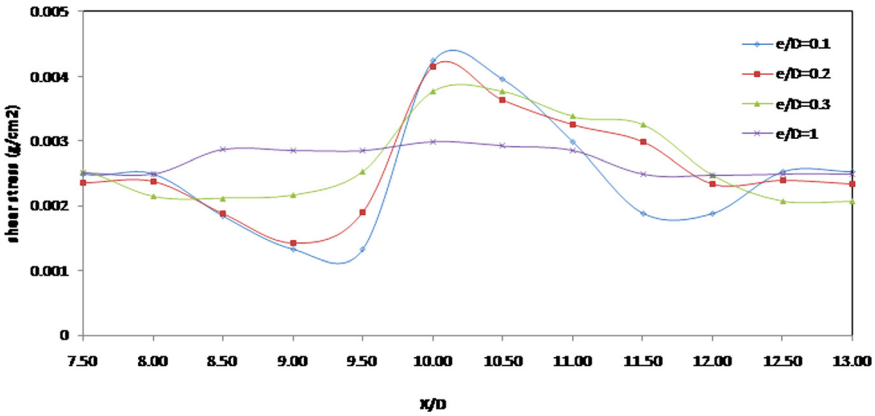

Fig. 7 Distribution of flow shear stress near the rigid bed at different gap ratios

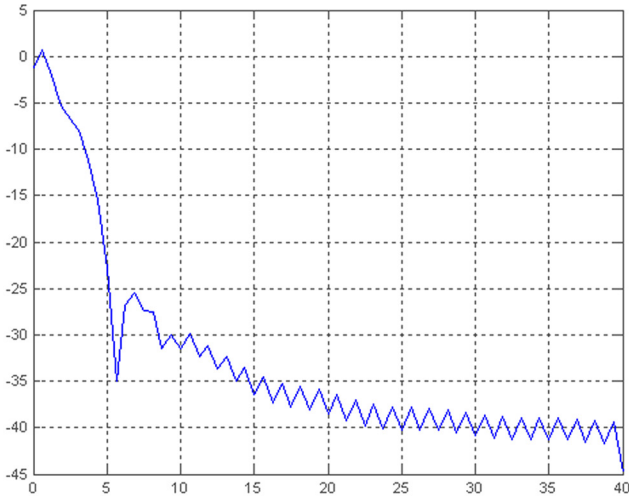

(a) upper side of pipe

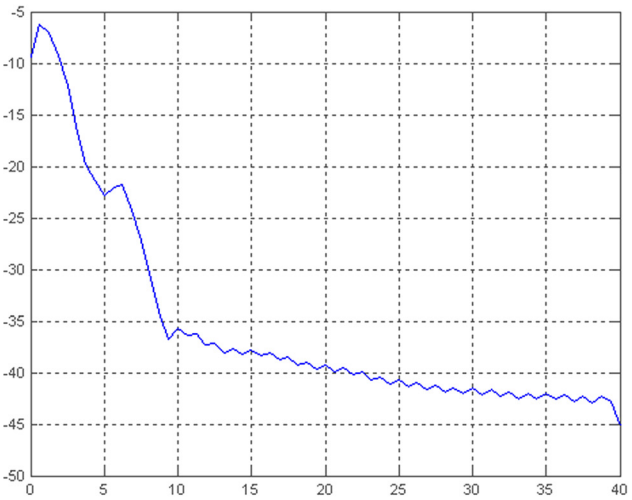

(b) lower side of pipe

Fig. 8 PSD diagram for horizontal velocity upper around a pipe: (*a*) upper side of pipe and (*b*) lower side of pipe

$$\frac{\pi d^4}{32}\frac{d\omega_{pi}}{dt} = \frac{d}{2}\sum_j [f_s] \tag{17}$$

$$C_D = C_{D\infty} + \frac{24}{\mathrm{Re}_p}, \quad C_{D\infty} = 0.4, \quad \mathrm{Re}_p = \frac{u_{pi}d}{\nu} \tag{18}$$

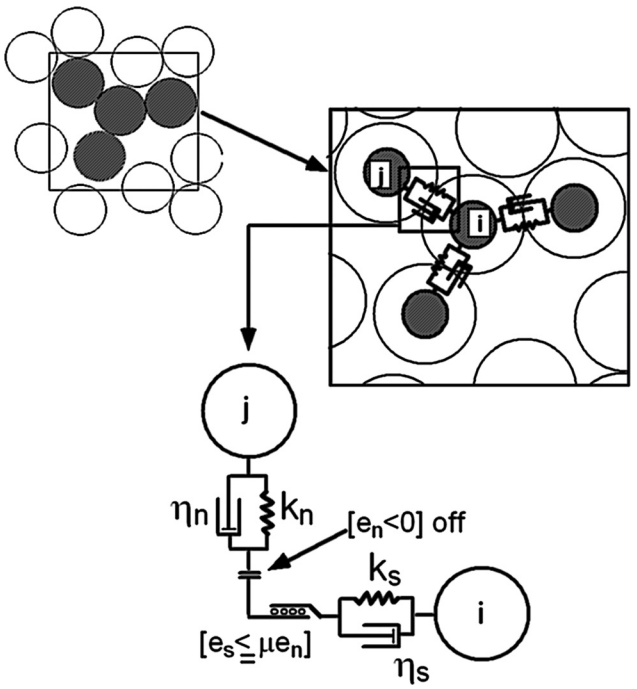

Fig. 9 Multiparticle collision and interaction system between each contacting grains in the DEM model [28]

in which A_2 and A_3 are two- and three-dimensional geometrical coefficients of the particle; C_M and C_D are, respectively, the added mass and drag coefficients; d is the particle diameter; u_{pi} and v_{pi} are horizontal and vertical components of the particle velocity; f_n and f_s are normal and tangential components of the force acting between the i_{th} and j_{th} particle on the n-s local coordinate system; x_i, y_i are coordinates of the i_{th} particle in the $x-y$ directions; f_{Dx_i} and f_{Dy_i} are sediment-fluid interactions terms in the horizontal and vertical directions for particle i, respectively; ω_π is the rotational angle of the i_{th} particle; Re_p is the sediment grain Reynolds number; and α_{ij} is the contacting angle between the i_{th} and j_{th} particles that equations of motion of the disk particles are solved in the explicit scheme presented in Fig. 9. The constants associated with the sediment phase model are reported in Table 2.

The interaction forces between the sediment and fluid phases were estimated based on the Newton third-law action and reaction hypothesis, in which the imposed forces to sediment particles at the fluid cell in the previous time step were transformed to the fluid domain in the next time step.

4.2 Interparticle Interaction. At the contacting point of each contact particle, the spring-dashpot system was introduced to

express the interparticle interaction, as shown in Fig. 9. As the sediment beneath the pipeline consists of the uniform sand grains, the assessment of contacting particle is formulated

$$\sqrt{(x_i - x_j)^2 + (y_i - y_j)^2} \le \gamma d \tag{19}$$

where (x_i, x_j) and (y_i, y_j) are the coordinates of centroid of i_{th} and j_{th} particles and γ is the constant around 1.0. The acting force in the normal and tangential directions between two contacting particles i_{th} and j_{th} can be estimated by following relations. The interaction terms in both the tangential and normal directions can be written as follows:

$$f_n(t) = e_n(t) + d_n(t); \quad f_s(t) = e_s(t) + d_s(t) \tag{20}$$

$$e_n(t) = e_n(t - \Delta t) + Ak_n.\Delta\varsigma_n; \quad d_n(t) = \eta_n.\Delta\varsigma_n/\Lambda t_s \tag{21}$$

$$e_s(t) = e_s(t - \Delta t) + Ak_s.\Delta\xi_s; \quad d_s(t) = \eta_s.\Delta\xi_s/\Delta t_s \tag{22}$$

where $e_n(t)$ and $e_s(t)$ are forces acting on the spring; $d_n(t)$ and $d_s(t)$ are forces acting on the dashpot; Ak_n and Ak_s are spring constants; η_n and η_s are damping constants; and $\Delta\zeta_n$ and $\Delta\zeta_s$ are displacements of a particle during the time marching in sediment phase Δt_s.

Since sand grains were assumed as noncohesive grains, a joint between contacting grains was not resisted against tension forces. On the other hand, a shear stress limit was utilized in the local tangential direction, and joint slips by exceeding this limit. The joint characteristics can be defined as

$$f_n(t) = f_s(t) = 0 \quad \text{when} \quad .e_n(t) < 0 \tag{23}$$

$$|f_s(t)| = \mu|e_n(t)| \quad \text{when} \quad |e_s(t)| > \mu|e_n(t)| \tag{24}$$

Here, μ is the coefficient of friction (=0.55). The time step Δt_s should be proportional to the critical time step or Δt_c to satisfy the DEM model stability. For a single mass-spring system with a single degree of freedom based on the particle mass m, Δt_s and Δt_c can be estimated as

$$\Delta t_s = \Delta t_c/20; \quad \Delta t_c = 2\pi\sqrt{m/2Ak_n} \tag{25}$$

The time-marching sediment phase was adopted as Δt_s; thus, Ak_n was estimated by Eq. (25) and Ak_s by the following equation:

$$Ak_s = \frac{Ak_n}{2(1 + \nu_{pos})} \tag{26}$$

The damping coefficients were estimated from the critical damping conditions,

$$\eta_n = \alpha_{cn} 2\sqrt{m.Ak_n}; \quad \eta_s = \frac{\eta_n}{2(1 + po)} \tag{27}$$

Here, po (= 0.3) is the Poisson's ratio and α_{cn} (= 1.0) is a calibrating coefficient. For more information, please refer to Yeganeh-Bakhtiary et al. [18].

4.3 Computational Domain and Boundary Conditions. In addition to the fluid phase, the boundary conditions for the sediment phase had to be specified. Figure 10 shows a schematic sketch of the computational domain to evaluate the scour beneath a pipe flow model along with its corresponding boundary conditions. According to Yeganeh-Bakhtiary et al. [18], in the sediment phase, the packing is essential to determine the initial position of sediment particles before starting calculations; thus, two different sets of particles in the packing procedure were defined, namely main sediment particles and solid wall particles. Main particles were initially arranged, leaving a $0.001d$ gap between each other. Prior to the main calculation phase, a preliminary packing procedure was executed to determine the locations of sediment particles. In other words, the sediment particles were subjected to gravity force in the packing process to fill initial porosity, leading to a more natural arrangement of bed particles. During the packing process, the velocity of moving particles was monitored to assess the convergence of the packing calculation.

A periodic boundary condition was assumed in the x-direction to facilitate the numerical simulation. In the sediment domain, to decrease the computational load as a particle moves out of the domain, the particle again reintroduced to the domain with the same characteristics from the other side of the periodic boundary. To prevent the particle penetration to the wall boundary, the stiffness coefficient for springs was selected two times more than the existing stiffness among the sediment particles. At the wall boundaries, the mechanical characteristics were set twice as the main particles, since these particles were set to have no displacement during interparticle contacts; therefore, the static contact characteristics were replaced with the kinetic ones as

$$k_n^{wall} = 2k_n; \quad k_s^{wall} = 2k_s; \quad \eta_n^{wall} = 2\eta_n;$$
$$\eta_s^{wall} = 2\eta_s; \quad \mu_{wall} = 2\mu \tag{28}$$

A great deal in the application of the MBS-2D model is the decrease of particle numbers to one that the model can readily run the program with less calculation load. To do so, considering representative particles, as long as the scour modeling process was not immersed by the size of particles, can be a very reasonable remedy for this deficiency. In this numerical experiment, the number of particles was set to 6240, with the size of 2 mm as the representative bed grain, while the average size of the sand grain in Mao's [5] experiment is 0.36 mm.

4.4 Simulation of Live-Bed Scour. Since application of a numerical model is completely dependent on its verification against a real life problem, herein the developed two-phase flow model was evaluated versus the experiment of Mao [5], used as a

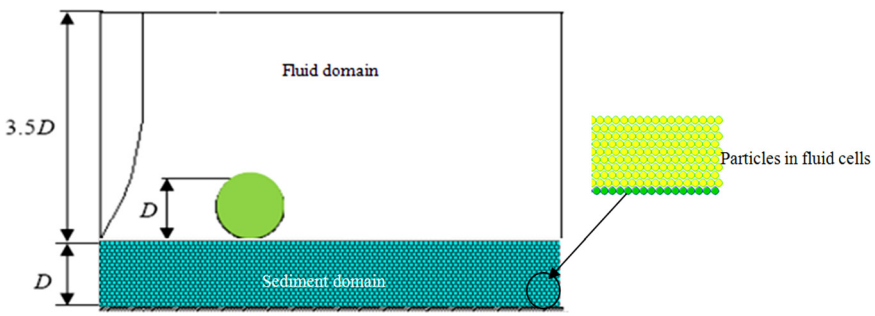

Fig. 10 Schematic sketch of computational domain of current-induced scour beneath a pipe

Table 3 Parameters in Mao's [5] experimental setup

Parameters	D (cm)	d_{50}(mm)	U(cm/s)	e/D	θ
Value	5	0.36	86.9	0	0.33

benchmark test for the modeling efforts. Hence, the following set up was chosen, in which the fluid phase domain was 0.5 m wide and 0.2 m deep, while the sediment phase was 0.5 m wide and the domain thickness was 0.05 m. The time increment in the fluid phase was chosen as 0.04 s (Δt), whereas, for the sediment phase, it was set to 10 E–5 (Δt_s). Table 3 reports the experiment hydrodynamics conditions of Mao [5].

To simulate the scour process with the MBS-2D model, the boundary shear velocity in the sediment phase domain was decreased by applying the periodic boundary and having fixed Shields parameters between the Mao's experiment [5] and the numerical simulation [27],

$$\theta = \frac{u_*^2}{(S-1)gd} \tag{29}$$

Here, u_* is the shear velocity, S is the relative sediment specific density ($=\rho_s/\rho$), and d is the sediment diameter.

As seen in Table 3, since $\theta > \theta_{cr}$, the live-bed condition in the experiment is met. Mao [5] reported that the scour process in the live-bed condition was not significantly influenced by the size of bed grains; hence, it can be inferred that, in the live-bed condition, the scour process mainly depends on the Shields parameter. That is because of the same transport condition near and far from the pipe, resulting in equal exchange of sediment discharge.

After development of the MBS-2D model and selecting the studied case, the simulated results obtained by the model were reported in different snapshots. It is noted that the time scales for the developed model and the observed laboratory data were significantly different, due to not considering the exact micromechanics of scour in both the tunnel erosion and lee-wake stages. Therefore, the bed evolution processes were scaled according to the equilibrium time of the scour process.

Figure 11 presents the bed evolution snapshots at different time steps, namely $t = 0$ min, $t = 11$ min, $t = 18$ min, $t = 25$ min, $t = 50$ min, and $t = 120$ min, respectively. As seen from the snapshots, the numerical model predicted the scour profile very well, though little discrepancies still existed on the rear side of the pipe.

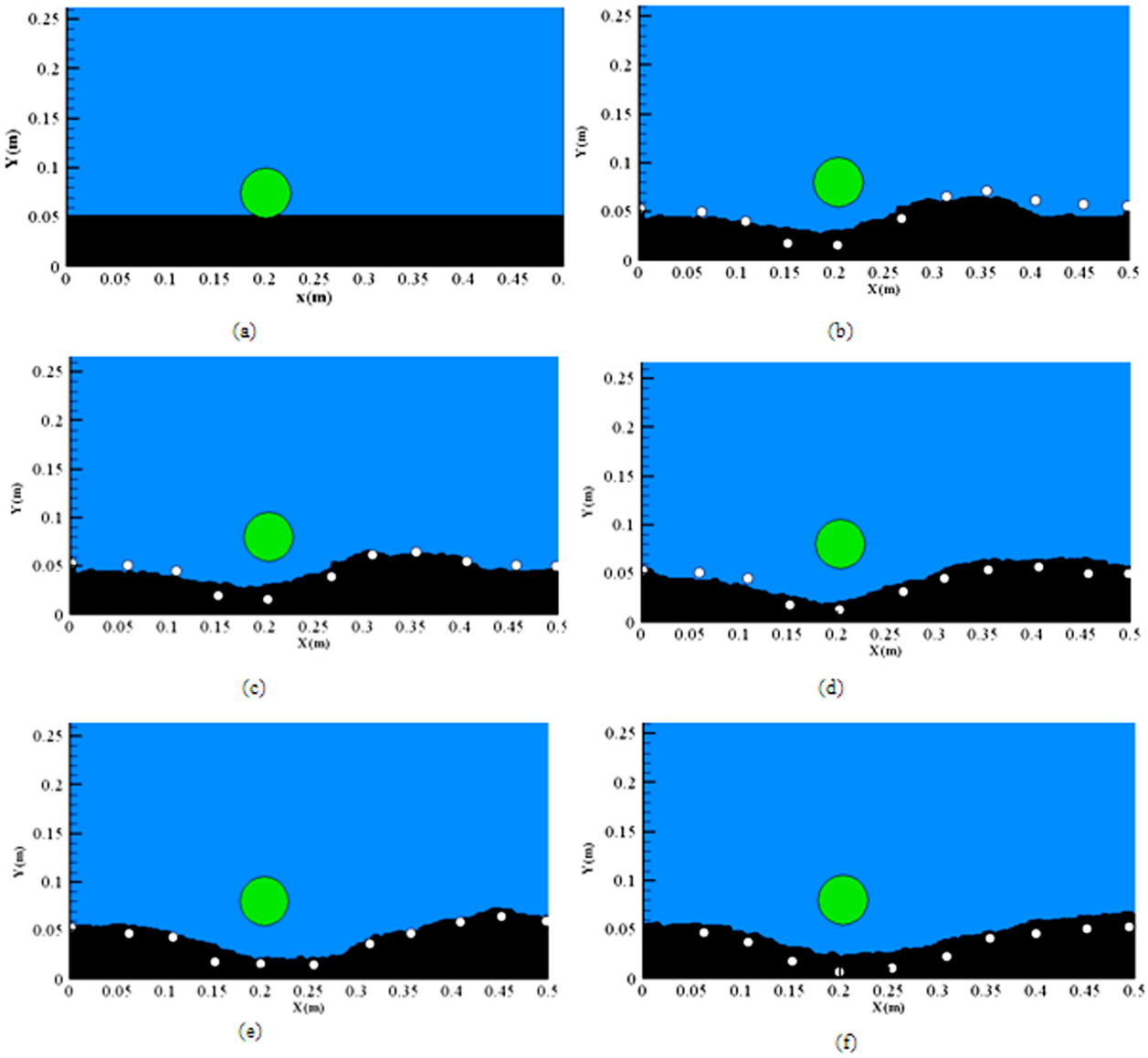

Fig. 11 Snapshots of bed profile during scouring beneath a pipe. The shadow is the simulated profiles and the solid circle is the Mao [5] observation at: (*a*) $t = 0$ min; (*b*) $t = 11$ min; (*c*) $t = 18$ min; (*d*) $t = 25$ min; (*e*) $t = 50$ min; (*f*) $t = 120$ min.

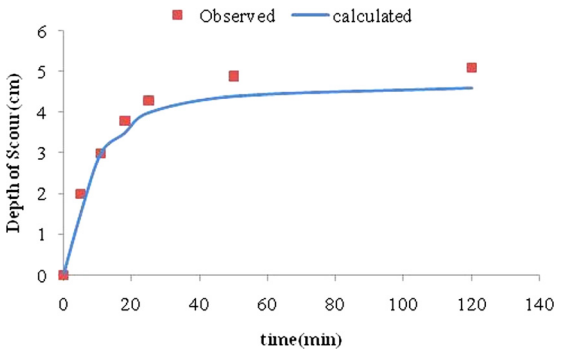

Fig. 12 Time-dependent scour depth and its comparison with Mao's [5] observation

This may be attributed to the complicated flow pattern that changes continuously, due to the generation and movement of the sediment mound as well as the one-way nature of the coupling between fluid and sediment phases. It can be inferred that, at the very beginning of tunnel erosion, the numerical model can simulate the generated dune at the rear side of the pipe, considering interactions among particles, pipe, and flow field. It is readily seen that the Euler–Lagrange coupling model does not need to use a sinusoidal profile at the initiation of scour. It means, unlike most of previous studies, in which a sinusoidal profile perturbation was assumed, in our model, the scour simulation starts from an initial flatbed profile under the pipe. The sinusoidal profile assumption, on the other hand, can cause some inaccuracy in simulation of the flow pattern and subsequently the scour profile, particularly at early stages. Another point that should be elaborated is the triangle shape of scour beneath the pipe induced by the larger amount of sediment immigration at the rear side than the front side of the pipe, which clearly indicates the effect of vortex shedding to trigger the sediment motion at the lee-wake stage of scour.

To explore the scour depth formation as one of the important issues to validate the performance of the MBS-2D model for simulation of the current-induced scour beneath a pipe, the time variation of scour depth obtained from the numerical simulation is compared with that of the Mao [5] results and depicted in Fig. 12. As seen from the figure, the MBS-2D model simulates the general trend of scour depth formation at the whole scour processing well. The predicted scour depth agrees very well with that of the experimental one at early scour stages; however, the numerical model slightly underestimates the scour depth as the time marching towards the equilibrium stages. In other words, the scour depth increased rapidly at the initial stages of scour, which corresponded to the tunnel erosion ($t < 10$ min). Thereafter, the scour depth increased at a progressively lower rate until it reached the equilibrium value: this finding is in line with the experimental results of Mao [5]. By revisiting Fig. 7 for distribution of fluid shear stress, it may be concluded that the reduction of the scour depth is closely correlated with the decrease in fluid shear stress at the scour hole beneath the pipe and on the upstream side of the scour mound. This finding is in line with the experimental observation reported by Mao [5] and later by Sumer and Fredsøe [23] on reducing the fluid shear stress beneath the pipe to reach its equilibrium value.

5 Conclusive Remarks

In this paper, an Euler–Lagrange coupling two-phase flow model was introduced to simulate the current-induced scour beneath marine pipelines. The simulation model, namely the MBS-2D model, was constructed with the RANS solver in conjunction with a k-ε turbulence closure model to describe the flow field around a pipe coupling to a Lagrange model based on the DEM for sediment phase motion. In the Euler–Lagrange coupling model, both the flow-particle and interparticle interactions were considered in a one-way coupling condition. At first, the fluid phase model was validated against the experimental studies of Alper Oner et al. [8] for current flow around a pipe over a fixed bed. Then, MBS-2D results were compared with the experimental data of Mao [5], which is usually used as a benchmark test for simulation of scour beneath a pipe. The result showed that the model performed well in comparison with the experimental data, and a very good agreement between the estimated profiles and observed ones was observed. The following conclusions can be drawn from this numerical study:

- The obtained result showed the capability of the fluid phase model to simulate the vortex shedding and estimated the range of both fluid shear stress and Strouhal number as the effective parameters in the scour process.
- The MBS-2D model predicted the scour profile very well, though little discrepancies existed on the rear side of the pipe. This may be attributed to the complicated flow pattern that changes continuously due to the generation and movement of the sediment mound as well as the one-way nature of the coupling between the fluid and sediment phases. It is evident from the numerical result that the triangle shape of the scour hole is induced by the larger amount of sediment immigration at the downstream side of the pipe to that of the upstream side, which clearly indicates the effect of vortex shedding to trigger the sediment motion around a marine pipeline at the lee-wake stage.
- The MBS-2D model simulates the general trend of scour depth formation at the whole scour processing well. The scour depth increased rapidly at the tunnel erosion stage of scour. Thereafter, the scour depth increased at a progressively lower rate until it reached the equilibrium value: this finding is in line with the experimental results of Mao [5]. The reduction of scour depth is closely correlated with the decrease in fluid shear stress at the scour hole beneath the pipe and on the upstream side of the scour mound.

Acknowledgment

The second author would like to express his gratitude toward Iran University of Science and Technology Deputy Research for their supports within the study.

Nomenclature

A_2, A_3 = two- and three-dimensional geometrical coefficient of particle
Ak_n and Ak_s = spring constants in tangential and normal directions
C_M = added mass coefficient
C_D = drag coefficient
C_μ, σ_k, σ_ε, $C_{1\varepsilon}$ $C_{2\varepsilon}$ = constants in the $k-\varepsilon$ turbulence model
D = pipe diameter
d = particle diameter
$d_n(t)$ and $d_s(t)$ = damping force acting on dashpot in tangential and normal directions
$e_n(t)$ and $e_s(t)$ = force acting on spring
e/D = the pipe's gap ratio
F_{Dx} and F_{Dy} = sediment-fluid interactions terms
f = vortex-shedding frequency
f_n, f_n = normal and tangential components of the interparticle force
g = acceleration of gravity
i_{th} and j_{th} = number of particle
k = turbulent kinetic energy
m = mass of particle
P = fluid pressure
po = Poisson's ratio
p_r = production of turbulent kinetic energy due to shear stress

Re_D = pipe's Reynolds number
S = sediment specific density
S_t = Strouhal number
t = marching time
U, V = the mean flow velocity components in horizontal and vertical directions
u_{pi}, v_{pi} = horizontal and vertical components of the particle velocity
u_* = boundary shear velocity
x_i, y_i = position of i_{th} particle
Δt = marching time step in fluid phase
Δt_c = critical time step
Δt_s = marching time step in sediment phase
Γ = effective viscosity
ν = molecular viscosity
ν_t = eddy viscosity
ε = dissipation of turbulent kinetic energy
η_n and η_s = damping coefficients in tangential and normal directions
$\Delta\zeta_n$ and $\Delta\zeta_s$ = displacements of a particle during time increment Δt_s
α_{ij} = contacting angle between i_{th} and j_{th} particles
τ_w = fluid shear stress along seabed

References

[1] Sumer, B. M., and Fredsøe, J., 1992, "A Review of Wave/Current-Induced Scour Around Pipelines," *Proc. 23th International Coastal Engineering Conference*, Venice, Italy, Vol. 3, pp. 2839–2850.
[2] Kjeldsen, S. P., Gjørsvik, O., Bringaker, K. G., and Jacobsen, J., 1973, "Local Scour Near Offshore Pipelines," Proc. of 2nd International Conference on Ports and Ocean Engineering Under Arctic Conditions, University of Iceland, pp. 308–331.
[3] Lucassen, R. J., 1984, "Scour Underneath Submarine Pipelines," Marine Tech. Res., The Netherlands, MATs Report No. PL-4 2A.
[4] Bearman, P. W., and Zdravkovich, M. M., 1978, "Flow Around a Circular Cylinder Near a Plane Boundary," J. Fluid Mech., **89**(1), pp. 33–47.
[5] Mao, Y., 1986, "The Interaction Between a Pipeline and an Erodible Bed," Ph.D. dissertation, Technical University of Denmark, Lyngby, Denmark.
[6] Mousavi, M. E., Yeganeh-Bakhtiary, A., and Enshaei, N., 2006, "Equilibrium Profile of Current-Induced Scour Around Submarine Pipelines," Proc. 25th International Conference on Offshore Mechanics and Arctic Engineering, ASME, Hamburg, Paper No. 92383.
[7] Dey, S., and Singh, N., 2008, "Clear-Water Scour Below Underwater Pipelines Under Steady Flow," J. Hydraul. Eng., **134**, pp. 588–600.
[8] Alper Oner, A., Salih Kirkgoz, M., and Sami Akoz, M., 2008, "Interaction of Current With Circular Cylinder Near Rigid Bed," Ocean Eng., **35**(14–15), pp. 1492–1504.
[9] Chao, J. L., and Henessy, P. V., 1972, "Local Scour Under Ocean Outfall Pipelines," J. Water Pollut. Control Fed., **44**(7), pp. 1443–1447.
[10] Li, F., and Cheng, L., 1999, "Numerical Model for Local Scour Under Marine Pipelines," J. Hydraul. Eng., **125**(4), pp. 400–406.
[11] Liang, D., and Cheng, L., 2005, "Numerical Modeling of Flow and Scour Below a Pipeline in Currents: Part I. Flow Simulation," Coastal Eng., **52**(1), pp. 25–42.
[12] Liang, D., Cheng, L., and Li, F., 2005, "Numerical Modeling of Flow and Scour Below a Pipeline in Currents: Part II. Scour Simulation," Coastal Eng., **52**(1), pp. 43–62.
[13] Dupuis, A., and Chopard, B., 2002, "Lattice Gas Modeling of Scour Formation Under Submarine Pipelines," J. Comput. Phys., **178**, pp. 161–174.
[14] Zhao, Z., and Fernando, H., 2007, "Numerical Simulation of Scour Around Pipelines Using an Euler–Euler Coupled Two-Phase Model," Environ. Fluid Mech., **7**, pp. 121–142.
[15] Yeganeh-Bakhtiary, A., Kazeminezhad, M. H., Etemad-Shahidi, A., Bass, H. M., and Cheng, L., 2011, "Euler-Euler Two-Phase Flow Simulation of Tunnel Erosion Beneath Marine Pipelines," Appl. Ocean. Res., **33**, pp. 137–146.
[16] Yeganeh, A., Gotoh, H., and Sakai, T., 2000, "Applicability of Euler-Lagrange Coupling Multi-Phase Flow to Bed-Load Transport Under High Bottom Shear," J Hydraul. Res., **38**, pp. 389–398.
[17] Calantoni, J., Puleo, J. A., and Todd Holland, K., 2006, "Simulation of Sediment Motion Using a Discrete Particle Model in Inner Surf and Swash Zones," Cont. Shelf Res., **26**, pp. 610–621.
[18] Yeganeh-Bakhtiary, A., Shabani, M., Gotoh, H., and Wang, S. M., 2009, "A Three-Dimensional Distinct Element Model for Bed-Load Transport," J. Hydraul. Res., **47**(2), pp. 203–212.
[19] Launder, B. E., and Spalding, D. B., 1974, "The Numerical Computation of Turbulent Flows," Comput. Methods Appl. Mech. Eng., **3**, pp. 269–289.
[20] Snider, D. M., O'Rourke, P. J., and Andrews, M. J., 1998, "Sediment Flow in Inclined Vessels Calculated Using a Multiphase Particle-in-Cell Model for Dense Particle Flows," Int. J. Multiphase Flow, **24**, pp. 1359–1382.
[21] Rodi, W., 1980, "Turbulence Models and Their Application in Hydraulics, a State of the Art Review," International Association for Hydraulic Research, Delft, The Netherlands, IAHR Publication No. 78.
[22] Liang, D., and Cheng, L., 2004, "Numerical Model for Wave-Induced Scour Below a Submarine Pipeline," J. Waterway, Port, Coastal, Ocean Eng., **131**(5), pp. 193–202.
[23] Sumer, B. M., and Fredsøe, J., 1991, "Onset of Scour Below a Pipeline Exposed to Waves," Int. J. Offshore Polar Eng., **13**, pp. 189–194.
[24] Price, S. J., Summer, D., Smith, J. G., Leong, K., and Paidoussis, M. P., 2002, "Flow Visualization Around a Circular Cylinder Near to a Plane Wall," J. Fluids Struct., **16**, pp. 175–191.
[25] Lin, W. J., Lin, C., Hsieh, S. C., and Dey, S., 2009, "Flow Characteristics Around a Circular Cylinder Placed Horizontally Above a Plane Boundary," J. Eng. Mech., **135**, pp. 697–716.
[26] Cundall, P. A., and Strack, O. D., 1979, "A Discrete Numerical Model for Granular Assembles," Geotechnique, **29**(1), pp. 511–523.
[27] Shields, A. V., 1936, *Anwendung der Ahnlichkeits Mechanik und der Turbulenz- forschung auf die Geschiebe Bewegung*, Mitteilungen Preuss, Versuchanstalt fur Wasserbau and Schiffbau, Berlin, p. 26.
[28] Gotoh, H., and Sakai, T., 1997, "Numerical Simulation of Sheet Flow as Granular Materials," J. Waterway, Port, Coastal, Ocean Eng., **123**(6), pp. 329–336.